ISSN 2616-5880 Vol. 7, Issue 1: 41-49, DOI: 10.25236/AJMC.2026.070107

Study on the Solute Dispersion Mechanism under the Coupling Effect of Fracture Geometric Parameters

Wanting Hu[1,a,*], Chenhao Li[1,b], Jiawen Cai[2,c]

[1]College of Science, China Jiliang University, Hangzhou, China
[a]hwt18949966146@163.com, [b]p23080854014@cjlu.edu.cn, [c]p24060858002@cjlu.edu.cn
[*]Corresponding author: hwt18949966146@163.com

Abstract: *Solute dispersion in natural fractures is critical for groundwater contamination prediction. Fracture geometry-particularly pore-throat ratio(R ($R=r_{max}/r_{min}$)), surface roughness(Ra), and average pore radius($\bar{r}$)-exerts significant but poorly understood coupled effects on dispersion. Using stochastically generated rough fracture models and COMSOL Multiphysics, this study simulates single fractures with varying R, Ra, and $\bar{r}$, and quantifies the longitudinal dispersion coefficient (D_l). Increasing R from 1 to 3.28 reduces D_l by up to 60% with nonlinear decay. Higher Ra enhances the effect; at Ra = 0.08 mm, the D_l decrease is nearly 20% greater than at Ra = 0.04 mm. A multivariate nonlinear regression model captures the synergistic parameter interactions and identifies the Ra·R coupling term as the dominant control. This work provides a theoretical foundation for contaminant transport assessment in fractured media.*

Keywords: *Solute transport, Fractured media, Dispersion coefficient, Coupling effect*

1. Introduction

Natural fractures are primary pathways for groundwater flow and solute transport[1], relevant to nuclear waste disposal[2], mining[3], and hydrocarbon recovery[4]. Predicting solute transport in fractures is essential for contamination prevention[3,5].The SF is the fundamental unit of fractured rock masses. Early studies assumed constant apertures and smooth walls, neglecting natural heterogeneity[6]. Later work introduced aperture variations and surface roughness. Hoagland & Prud'homme[7] showed that periodic pore contraction and expansion strongly affect dispersion. Keller et al. [8] confirmed that dispersion is geometry-controlled at high velocities. Bouquain et al.[9] reported that boundary fluctuations can increase dispersion by up to 12 times Taylor-Aris values.

Natural fractures exhibit stochastic aperture distributions[10].Numerical simulations[11] revealed enhanced vortex development and nonlinearity with increasing *Re*.Gelhar[12] found that roughness consistently increases dispersion. Dronfield and Silliman[13] observed a power-law relationship between dispersion coefficient and velocity. However, non-uniform fractures generate complex pore structures and multiple flow paths, leading to stronger mixing and dispersion. Dejam M et al.[14] compared stochastic and periodic roughness models. A DFN-based study[15] developed a coupled 2D flow and transport model and reported that local aperture variations cause concentration fluctuations of 0.5%-30%, significantly affecting transport behavior.

Most existing studies have examined roughness or aperture variation separately, leaving their coupled effects poorly understood. Systematic research on how non-uniform apertures and roughness jointly regulate flow structure, vortex evolution, and dispersion remains scarce. To address this gap, this study constructs a series of single-fracture numerical models with randomly distributed apertures and controllable roughness. Focusing on the synergistic effects of pore-throat ratio, roughness height, and average aperture, it aims to reveal the multi-factor coupling mechanisms governing dispersion and transport, providing theoretical support for groundwater contamination assessment and remediation in fractured media.

ISSN 2616-5880 Vol. 7, Issue 1: 41-49, DOI: 10.25236/AJMC.2026.070107

2. Materials and Methods

2.1. Rough Fracture Geometric Model

The SF geometric model constructed adopts typical values of *Ra*, *R*, and $\bar{r}$ from references [16-17].*Ra* is defined as:

$$Ra=\frac{1}{n}\sum_{i=1}^{n}|y_i-\bar{y}| \tag{1}$$

where y_i is the height value, $\bar{y}$ is the average height of the surface, and *n* is sampling points number. Fracture length *L* is 10 mm with sampling interval Δx=0.01 mm(*N*=1000). Geometries are generated via a parametric algorithm based on a real rough fracture profile[18] , adjusting the upper wall to control $\bar{r}$, *R*, and *Ra* while preserving original statistical characteristics. Lower wall roughness is fixed at *Ra*=0.04mm. Parameter settings are shown in Table 1.

Table 1: Basic geometric parameters of rough fractures.

Fractures		$\bar{r}$(mm)	*R*	*Ra*(mm)
F1	F1-1	0.3	1	0.04
	F1-2		1.9	
	F1-3		2.56	
	F1-4		3.28	
F2	F2-1	0.4	1	0.04
	F2-2			0.06
	F2-3			0.08
F3	F3-1		1.9	0.04
	F3-2			0.06
	F3-3			0.08
F4	F4-1		2.56	0.04
	F4-2			0.06
	F4-3			0.08
F5	F5-1		3.28	0.04
	F5-2			0.06
	F5-3			0.08
F6	F6-1	0.5	1	0.04
	F6-2		1.9	
	F6-3		2.56	
F7	F7-1	0.6	1	0.04
	F7-2		1.9	
	F7-3		2.56	

2.2. Solute Transport Model

The physical mechanisms of solute transport in fractured rock masses mainly include advection, dispersion, and diffusion[12]. This paper focuses solely on advection and dispersion. Fluid properties follow standard water values at 20°*C*, and the basic assumptions are as follows:

(1) Both fluid and solid phases are incompressible; the fluids are first-contact miscible.

(2) The aqueous phase fluid is considered Newtonian.

(3) Chemical reactions and sorption between the two fluids are not considered.

(4) The diffusion coefficient is assumed constant and isotropic throughout the displacement process.

(5) The gravity effects of the two fluids are neglected.

The governing equations include the mass conservation equation (Equation (2)), the Navier-Stokes equations (Equation (3)), and the advection-diffusion equation (Equation (4)).

$$\nabla\cdot u=0 \tag{2}$$

ISSN 2616-5880 Vol. 7, Issue 1: 41-49, DOI: 10.25236/AJMC.2026.070107

$$\rho\frac{\partial u}{\partial t}+\rho(u\cdot\nabla)u=-\nabla p+\nabla\cdot(\mu\nabla u) \tag{3}$$

$$\frac{\partial c}{\partial t}+u\cdot\nabla c=\nabla\cdot(D\nabla c) \tag{4}$$

Here, u is the fluid velocity (m/s), ρ is the mixture density (kg/m³), t is time (s), p is pressure (Pa), μ is dynamic viscosity (Pa·s), c is concentration (mol/m³), and D is the diffusion coefficient (m²/s).

The governing equations were solved using COMSOL Multiphysics based on the finite element method. Standard water properties at 20°C were used: ρ = 998.2 kg/m³, μ = 1.010×10⁻³Pa·s, and D= 1×10⁻⁶m²/s). Initial and boundary conditions are set as shown in Figure 1.

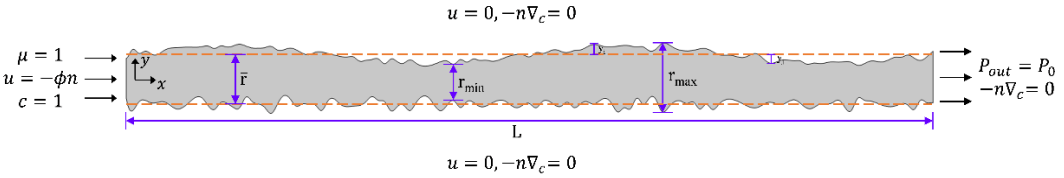

Figure 1: Schematic diagram of initial and boundary conditions for a rough fracture.

The initial conditions are set as follows:

$$u,c,p(x,t)|_{t=0}=0 \tag{5}$$

The wall, top, and bottom boundaries are set to *no*-slip and no-flux conditions, as shown below:

$$u=0 \tag{6}$$

$$-\boldsymbol{n}\cdot\nabla c=0 \tag{7}$$

Here, $\boldsymbol{n}$ is the unit normal vector of the boundary.

The left-hand inlet has a constant concentration flux, as shown below:

$$\left(-D\frac{\partial c}{\partial x}+uc\right)|_{x=0}=u_0c_0 \tag{8}$$

Here, c_0 is the inlet concentration (1 mol/m³), and u_0 is the solute injection velocity (0.1 m/s). The displacement process under different injection velocities can be simulated by adjusting u_0.

The export conditions are set as follows:

$$p_{out}=p_0 \tag{9}$$

The Pe is a dimensionless number commonly used in the study of transport phenomena, and it is usually defined as follows:

$$Pe=\frac{\overline{u}r_{min}}{D} \tag{10}$$

Here, $\overline{u}$ is the average convective velocity (m/s), and r_{min} is the minimum fracture aperture (m).

2.3. Longitudinal Dispersion Coefficient

The D_L was inversely determined by fitting the simulated spatiotemporal concentration data. The 2D concentration field $c(x,y,t)$ was first averaged along the y-direction at each x position using the velocity field $u(x,y,t)$. The resulting 1D concentration profile was then fitted with the analytical solution of the advection–dispersion equation to obtain D_L, as follows:

$$\overline{c}(x,t)=\frac{\int u(x,y,t)c(x,y,t)dy}{\int u(x,y,t)dy} \tag{11}$$

Here, u is the velocity component in the flow direction (m/s), and c is the average concentration in the y direction. Subsequently, the analytical solution of the one-dimensional advection-dispersion equation (ADE) is used to fit the breakthrough curve:

ISSN 2616-5880 Vol. 7, Issue 1: 41-49, DOI: 10.25236/AJMC.2026.070107

$$\frac{\partial c}{\partial t}=D_L\frac{\partial^2 c}{\partial x^2}-\bar{u}\frac{\partial c}{\partial x} \tag{12}$$

Its analytical solution is:

$$c(x,t)=c_0\left\{\begin{array}{l}\frac{1}{2}erfc\left(\frac{x-\bar{u}t}{2\sqrt{D_L t}}\right)+\sqrt{\frac{\bar{u}^2 t}{\pi D_L}}exp\left[-\frac{(x-\bar{u}t)^2}{4D_L t}\right] \\ -\frac{1}{2}[1+\frac{x}{D_L}+\frac{t}{D_L}]exp\left(\frac{\bar{u}x}{D_L}\right)erfc\left(\frac{x+\bar{u}t}{2\sqrt{D_L t}}\right)\end{array}\right\} \tag{13}$$

Here, *erfc* is the complementary error function. Using the SciPy optimization module in Python (version 3.11), the least squares method is employed to invert D_L, and the solution with the smallest mean squared error is selected as the final result.

Both pathwise(D_L) and local outlet(D_l) longitudinal dispersion coefficients were computed, with primary focus on D_l.

2.4. Model Verification

Meshing uses refined quadrilaterals at rough walls and aperture transition and free triangulars elsewhere. Grid independence was verified with four meshes, as shown in Fig. 2. The 31,511-element mesh yielded stable results, with relative differences below 0.1% and was adopted for all simulations.

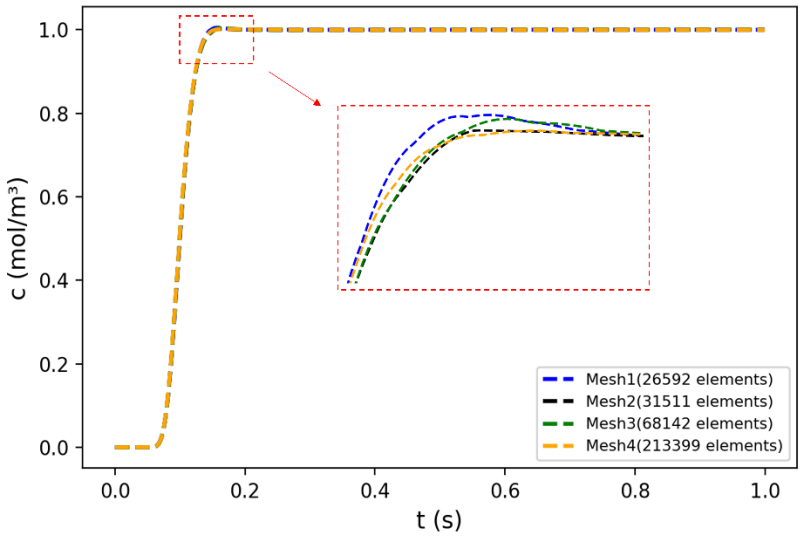

Figure 2: Grid independence test.

The numerical method was validated against the parallel-plate model using the analytical expression $D_L/D=1+00.019Pe^2$[19].Simulation results from seven test cases show good agreement with theoretical predictions (Fig. 3), confirming the accuracy of the numerical approach.

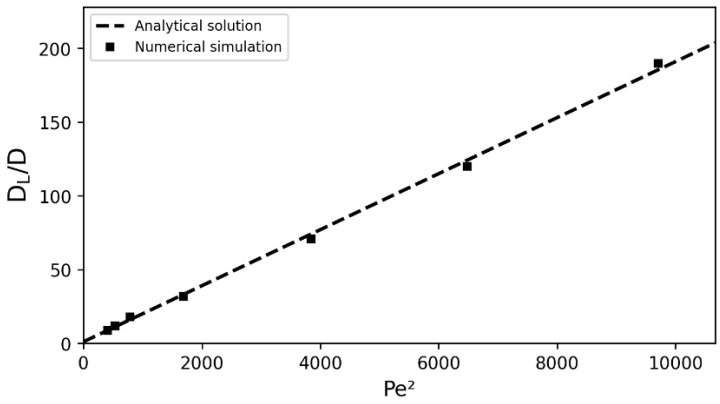

Figure 3: Validation of numerical method against parallel-plate analytical solution.

ISSN 2616-5880 Vol. 7, Issue 1: 41-49, DOI: 10.25236/AJMC.2026.070107

3. Results and Analysis

3.1. Velocity Distribution Characteristics in Rough Fractures

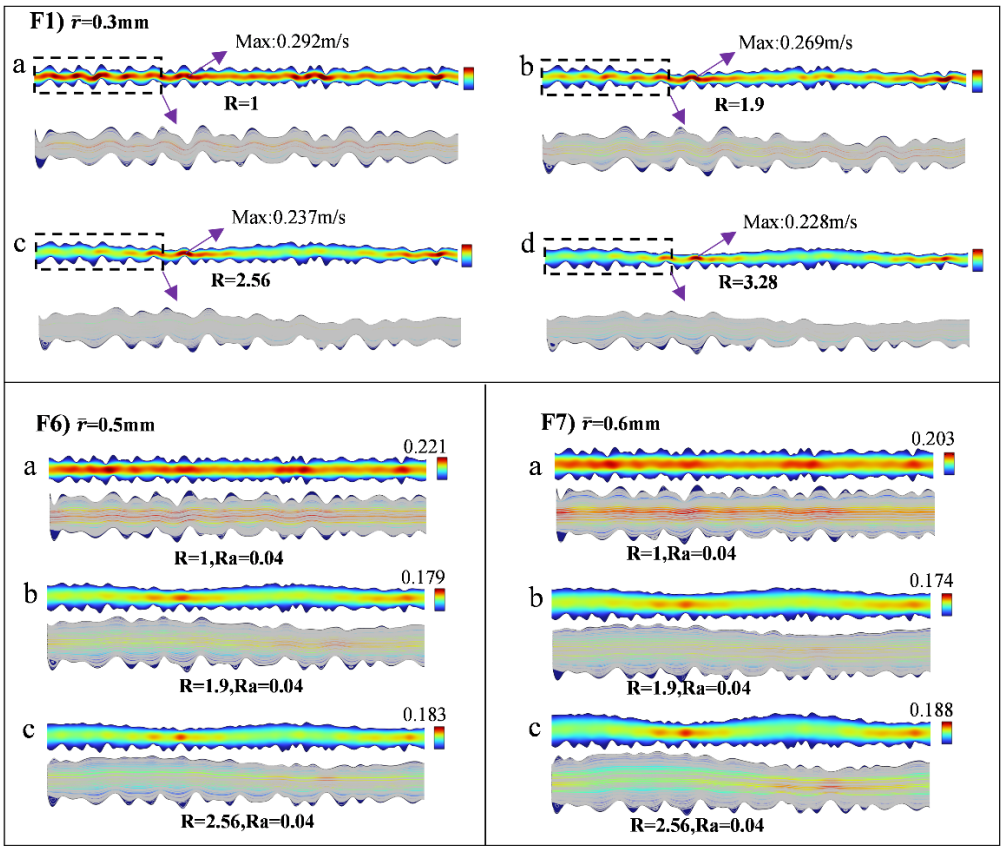

Figure 4: Velocity and streamline fields in SF at different R.

After the simulation reaches steady state, the velocity distribution and streamline structure in different SF models are obtained(Fig. 4). The $\bar{r}$ regulates the flow velocity in non-uniform aperture SF: increasing the aperture widens the main flow channels, accompanied by a decrease in velocity, thereby prolonging solute transport distance and causing earlier solute breakthrough at the outlet.

As upper wall roughness increases (Fig. 5 F2a-F2c), vortices increase, streamlines bend and converge toward walls. Maximum velocity rises with roughness. Lower roughness widens the main channel, reduces friction loss, and decreases maximum velocity. In non-uniform fractures (F4), maximum velocity variation is 40% smaller than in uniform fractures (F2), indicating a muted response to roughness. Pore-throat structures inherently create velocity heterogeneity; roughness adds secondary vortices in high-shear zones, dissipating energy and narrowing extreme velocity ranges.

Maximum velocity occurs at the narrowest aperture. Non-uniformity reduces it by 19% (Ra = 0.04) and ~30% (Ra = 0.06-0.08) due to higher flow resistance. The velocity gap between non-uniform and uniform fractures widens with roughness: from 0.046 (Ra = 0.04) to 0.124 (Ra = 0.08), 170% increase.

ISSN 2616-5880 Vol. 7, Issue 1: 41-49, DOI: 10.25236/AJMC.2026.070107

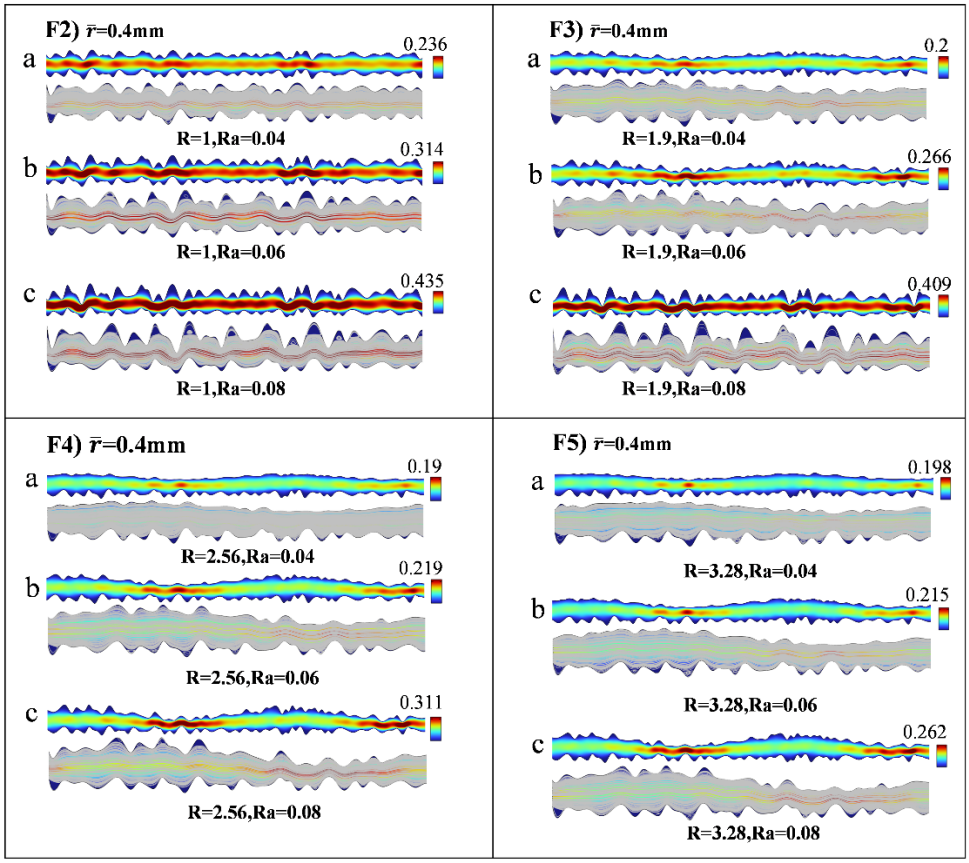

Figure 5: Velocity and streamline fields in SF at varying R, Ra, and $\bar{r}$ ($\bar{r}$=0.4 mm).

3.2. Concentration Distribution Characteristics in Rough Fractures

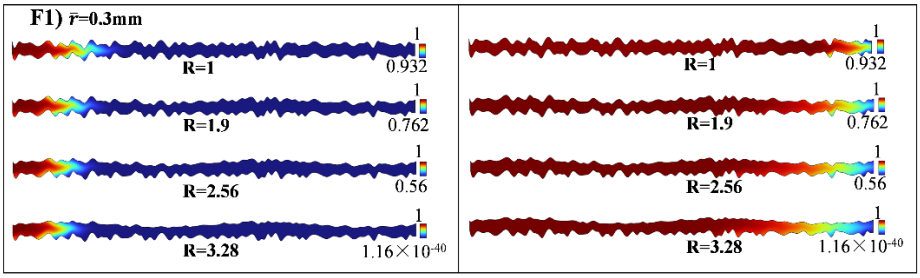

Figure 6: Inlet and outlet concentration profiles in SF.

As *R* increases, fracture complexity intensifies, producing dual effects on solute transport: reduced transport efficiency (shorter migration distance, delayed breakthrough) and enhanced solute–matrix interaction (increased local diffusion and dilution) (Fig. 6). These mechanisms collectively reduce the D_L in non-uniform fractures (Fig. 8a). The accompanying reduction in tailing distance shortens pollutant residence time, providing insights into solute transport behavior in such fractures.

Higher surface roughness *Ra* accelerates advection-dispersion and increases solute transport distance[8,10].As shown in Fig. 5 (F3), the velocity variation range at *Ra*=0.08 is twice that at *Ra*=0.04. Roughness elements distort the pore topology and concentration front, with disturbance intensity increasing with roughness height (Fig. 7, F2–F3). Under various pore-throat ratios, the dispersion coefficient consistently increases with roughness, indicating enhanced dispersion capacity (Fig. 10*b*)).

These results indicate that roughness, pore-throat ratio, and aperture jointly influence solute dispersion by regulating average flow velocity.

ISSN 2616-5880 Vol. 7, Issue 1: 41-49, DOI: 10.25236/AJMC.2026.070107

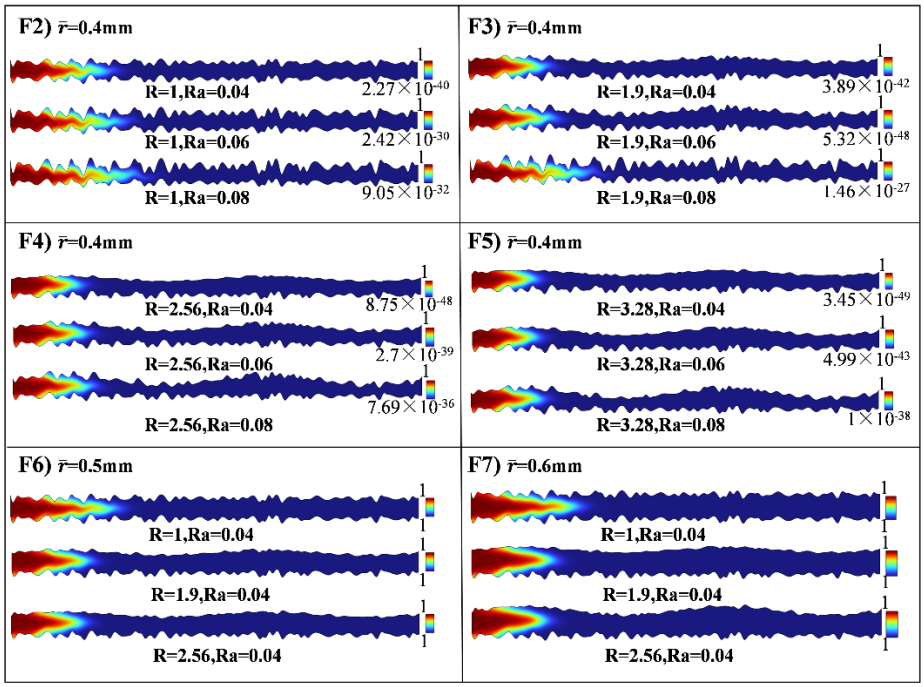

Figure 7: Concentration fields in SF under coupled R, Ra, and $\bar{r}$ conditions.

3.3. Longitudinal Dispersion Coefficient in Rough Fractures

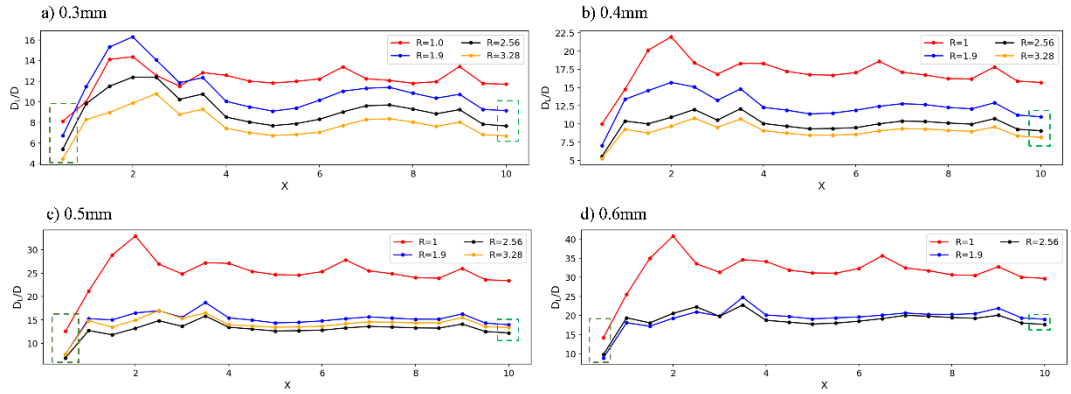

Figure 8: Longitudinal dispersion coefficient ratio along flow path at various R.

The fluctuation of D_L/D along the flow path is governed by fracture structural complexity, which distorts the displacement front via altered velocity and concentration gradients. At steady state (Fig. 8), aperture size shows negligible effect, while R inversely correlates with D_L/D. Larger apertures initially enhance molecular diffusion (Fig. 4), and greater aperture non-uniformity (e.g., F1d) disturbs the concentration front, increases diffusion area, and reduces dispersion (Fig. 7).

For $\bar{r}$=0.6 mm, D_l/D differs minimally between F8b and F8c, converging near 13, likely due to minor velocity differences. Other apertures exhibit clearer dispersion contrasts due to heterogeneity-induced front instability. Non-uniform fractures consistently yield lower dispersion than uniform ones.

Additionally, inlet-near D_l instability occurs from rapid initial concentration attainment, reducing early-stage solution consistency.

Based on all simulation results, an empirical exponential model was developed to quantify the coupled effects of R, Ra, and $\bar{r}$ on D_l/D (Fig. 9). Multivariate nonlinear regression yielded the following expression, which captures the nonlinear parameter interactions:

$$\frac{D_l}{D} = 1.623 \cdot exp(3.462\bar{r} - 0.026R + 29.422Ra - 0.260\bar{r} \cdot R - 4.543Ra \cdot R) \quad (14)$$

ISSN 2616-5880 Vol. 7, Issue 1: 41-49, DOI: 10.25236/AJMC.2026.070107

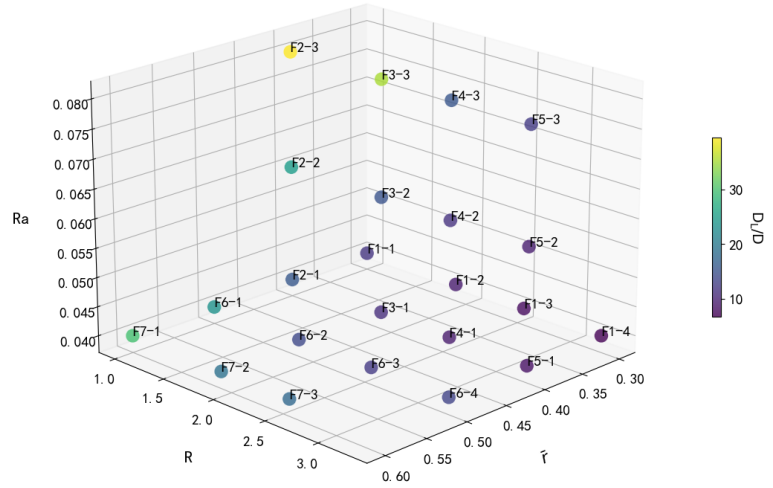

Figure 9: Coupled effects of R, Ra, and $\bar{r}$ on D_l/D.

The model exhibits high predictive accuracy ($R^2 = 0.9219$, and $RMSE = 2.41$). The independent effect coefficients indicate that $\bar{r}$(3.462) and Ra(29.422) enhance dispersion, while R (-0.0260) mildly inhibits it. Coupling analysis shows antagonistic effects for $\bar{r}\cdot R$(-0.260) and strong inhibition for $Ra\cdot R$ (-4.543). Influence ranking based on coefficient magnitude is: $Ra\cdot R > Ra > \bar{r} > \bar{r}\cdot R > R$, confirming the roughness–pore-throat coupling as the dominant factor controlling dispersion.

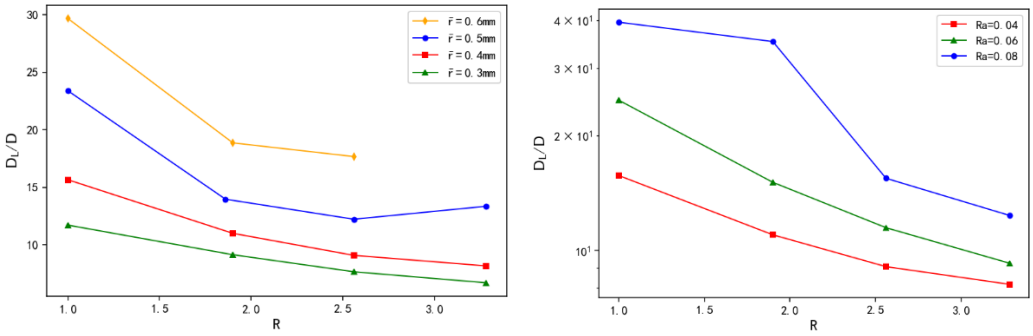

Figure 10: a)D_l/D versus R at different $\bar{r}$ (Ra=0.04 mm);b)D_l/D versus R at different Ra ($\bar{r}$=0.4 mm).

As shown in Fig. 10a, D_l decreases with increasing R at a diminishing rate. At $\bar{r}$=0.4 mm, raising R from 1 to 1.9, 1.9 to 2.56, and 2.56 to 3.28 reduces D_l by 30%, 18%, and 10%, respectively. This slowdown stems from reduced velocity and increased micro-vortices that prolong solute residence. Non-uniform fractures thus yield lower D_l than uniform ones, with reductions tapering at higher non-uniformity. At $\bar{r}$=0.3 mm, corresponding reductions are 22%,16%, and12%, indicating larger $\bar{r}$ amplifies R-induced suppression. At fixed Ra = 0.04 mm, increasing $\bar{r}$ from 0.3 to 0.6 mm raises D_l by 34-49% for R=1, and more substantially for non-uniform cases (e.g., R=1.9: 21-35%; R=2.56: 19-45%; R=3.28: 22-63%). This confirms that $\bar{r}$ enhances dispersion more strongly in non-uniform fractures.

As shown in Fig. 10*b*), higher R yields lower D_l an effect amplified by roughness. As Ra =0.04 mm, D_l drops by 30%, 18%, and 10% across the same R intervals; at Ra=0.06 mm, reductions rise to 39%, 24%, and 14%. Increased roughness thus significantly intensifies the inhibitory effect of R on dispersion.

4. Conclusions

This study investigates the coupled effects of R, Ra, and $\bar{r}$ on the D_l in single fractures, and establishes an empirical predictive model. Key findings:

(1) Pore-throat structure dominates dispersion inhibition. Increasing R from 1 to 3.28 reduces D_l by up to 60%, with nonlinear saturation. Independent coefficient: –0.026.

(2) Roughness exhibits dual effects. Independently, it enhances dispersion (coefficient: 29.422); coupled with R, it strongly inhibits dispersion (coefficient: –4.543). Increasing Ra from 0.04 to 0.08 mm

ISSN 2616-5880 Vol. 7, Issue 1: 41-49, DOI: 10.25236/AJMC.2026.070107

boosts D_l reduction by nearly 20%.

(3) Larger average aperture enhances dispersion. Increasing $\bar{r}$ from 0.3 to 0.6 mm raises D_l by up to 49%. Independent coefficient: 3.462.

(4) The empirical model quantifies parameter weights. The *Ra·R* coupling term is the dominant factor affecting dispersion.

(5) Geometric heterogeneity restructures flow fields. Non-uniform fractures show 40% smaller velocity variation and lower D_l than uniform fractures, leading to delayed breakthrough and short tailing.

This study quantifies the independent and coupled effects of key geometric parameters, enabling rapid dispersion estimation from basic geometric inputs and providing theoretical support for groundwater contamination assessment and remediation.

References

[1] Bodin J, Delay F, De Marsily G. Solute transport in a single fracture with negligible matrix permeability: 2. mathematical formalism[J]. Hydrogeology Journal, 2003, 11(4): 434-454.
[2] Cassell J S, Williams M M R. An integro-differential equation arising in radionuclide transport through fractured rock[J]. Mathematical Models and Methods in Applied Sciences, 1993, 3(5): 641-654.
[3] Jones T A, Detwiler R L. Mineral precipitation in fractures: using the level-set method to quantify the role of mineral heterogeneity on transport properties[J]. Water Resources Research, 2019, 55(5): 4186-4206.
[4] Zhao Z, Jing L, Neretnieks I, et al. Numerical modeling of stress effects on solute transport in fractured rocks[J]. Computers and Geotechnics, 2011, 38(2): 113-126.
[5] Boutt D F, Grasselli G, Fredrich J T, et al. Trapping zones: the effect of fracture roughness on the directional anisotropy of fluid flow and colloid transport in a single fracture[J]. Geophysical Research Letters, 2006, 33(21): 2006GL027275.
[6] Bodin J, Delay F, De Marsily G. Solute transport in a single fracture with negligible matrix permeability: 1. fundamental mechanisms[J]. Hydrogeology Journal, 2003, 11(4): 418-433.
[7] Hoagland D A, Prud'Homme R K. Taylor-Aris dispersion arising from flow in a sinusoidal tube[J]. AIChE Journal, 1985, 31(2): 236-244.
[8] Keller A A, Roberts P V, Kitanidis P K. Prediction of single phase transport parameters in a variable aperture fracture[J]. Geophysical Research Letters, 1995, 22(11): 1425-1428.
[9] Bouquain J, Méheust Y, Bolster D, et al. The impact of inertial effects on solute dispersion in a channel with periodically varying aperture[J]. Physics of Fluids, 2012, 24(8): 083602.
[10] Li B, Mo Y, Zou L, et al. Influence of surface roughness on fluid flow and solute transport through 3D crossed rock fractures[J]. Journal of Hydrology, 2020, 582: 124284.
[11] Zhang Q, Luo S, Ma H, et al. Simulation on the water flow affected by the shape and density of roughness elements in a single rough fracture[J]. Journal of Hydrology, 2019, 573: 456-468.
[12] Gelhar L W. Stochastic subsurface hydrology from theory to applications[J]. Water Resources Research, 1986, 22(9S): 135S-145S.
[13] Dronfield D G, Silliman S E. Velocity dependence of dispersion for transport through a single fracture of variable roughness[J]. Water Resources Research, 1993, 29(10): 3477-3483.
[14] Dejam M, Hassanzadeh H, Chen Z. Shear dispersion in a rough-walled fracture[J]. SPE Journal, 2018, 23(5): 1669-1688.
[15] Geetha Manjari K, Sivakumar Babu G L. Reliability and sensitivity analyses of discrete fracture network based contaminant transport model in fractured rocks[J]. Computers and Geotechnics, 2022, 145: 104674.
[16] Ozgumus T, Mobedi M. Effect of pore to throat size ratio on thermal dispersion in porous media[J]. International Journal of Thermal Sciences, 2016, 104: 135-145.
[17] Zhang S, Liu X, Wang E. Quantitative evaluation of the onset and evolution for the Non-Darcy behavior of the partially filled rough fracture[J]. Water Resources Research, 2024, 60(3): e2023WR036494.
[18] Chen Y F, Zhou J Q, Hu S H, Hu R, Zhou C B. Evaluation of Forchheimer equation coefficients for non-Darcy flow in deformable rough-walled fractures[J]. Journal of Hydrology, 2015, 529(3): 993-1006.
[19] Berkowitz B, Zhou J. Reactive solute transport in a single fracture[J]. Water Resources Research, 1996, 32(4): 901-913.